

Fractional quantum mechanics in polariton condensates with velocity-dependent mass

F. Pinsker,^{1,*} W. Bao,² Y. Zhang,^{3,4} H. Ohadi,⁵ A. Dreismann,⁵ and J. J. Baumberg⁵

¹*Department of Physics, Clarendon Laboratory, University of Oxford, Parks Road, Oxford OX1 3PU, United Kingdom*

²*Department of Mathematics, National University of Singapore, 119076 Singapore*

³*Beijing Computational Science Research Center, Beijing 100084, People's Republic of China*

⁴*Université de Rennes 1, IRMAR, Campus de Beaulieu, 35042 Rennes Cedex, France*

⁵*Department of Physics, Cavendish Laboratory, University of Cambridge, Cambridge CB3 0HE, United Kingdom*

(Received 14 August 2015; revised manuscript received 9 October 2015; published xxxxxx)

We introduce and analyze a mean-field model for polariton condensates which includes a velocity dependence of the effective polariton mass due to the photon and exciton components. The effective mass depends on the in-plane wave vector \mathbf{k} , which at the inflection point of the lower polariton energy branch becomes infinite, and above this becomes negative. The polariton condensate modes of this mean-field theory are now sensitive to mass variations and, for certain points of the energy dispersion, the polariton condensate mode represents fractional quantum mechanics. The impact of the generalized kinetic-energy term is elucidated by numerical studies in two dimensions showing significant differences for large velocities. Analytical expressions for plane-wave solutions as well as a linear waves analysis show the significance of this model.

DOI: [10.1103/PhysRevB.00.005300](https://doi.org/10.1103/PhysRevB.00.005300)

PACS number(s): 67.10.Hk, 03.75.Kk, 67.25.D-, 67.85.Jk

I. INTRODUCTION

About two decades ago, the fractional Schrödinger equation (FSE) was discovered as a mathematical extension within the Feynman path-integral formalism by transposing Brownian with Lévy-type paths [1,2]. This generalization of the fundamental equation of single-body quantum mechanics has given rise to new intriguing mathematical structures and forms the base of *fractional quantum mechanics* [1–6]. The FSE incorporates the concept of an intrinsically nonlocal *fractional* kinetic energy,

$$\begin{aligned} (-\Delta)^s f(\mathbf{r}) &\equiv \mathcal{F}^{-1}[|\mathbf{k}|^{2s} \mathcal{F}(f)] \\ &= \frac{1}{(2\pi)^d} \int_{\mathbb{R}^d} |\mathbf{k}|^{2s} \hat{f}(\mathbf{k}) e^{i\mathbf{k}\cdot\mathbf{r}} d\mathbf{k}, \end{aligned} \quad (1)$$

while the linear SE is the special case $s = 1$. $\mathcal{F}(f) \equiv \hat{f}(\mathbf{k}) = \int_{\mathbb{R}^d} f(\mathbf{r}) e^{-i\mathbf{k}\cdot\mathbf{r}} d\mathbf{r}$ denotes the Fourier transform of $f(\mathbf{r}) = \frac{1}{(2\pi)^d} \int_{\mathbb{R}^d} \hat{f}(\mathbf{k}) e^{i\mathbf{k}\cdot\mathbf{r}} d\mathbf{k}$. On the other hand, the concept of velocity-dependent mass is well established in solid-state physics [7], suggesting a possible route for the implementation of fractional quantum mechanics or even more complex kinetic energies, as will be shown in this paper utilizing polariton condensates.

To introduce the concept of generalized kinetic energy, we turn to the solid-state system of polariton Bose-Einstein condensates (BECs)—macroscopically occupied single-mode states that highlight properties of fundamental quantum mechanics, ranging from quantum harmonic oscillators [8,9] to interference [10,11], while providing control over key system parameters [12–15]. We show that the type of kinetic energy in Schrödinger-like models is of fundamental importance for the modes and particularly for nonequilibrium polariton condensate behavior at different locations of the dispersion. Polariton condensates have kinetic energies of the mathematical form of a Fourier multiplier, $\mathcal{F}^{-1}[g(\mathbf{k})\mathcal{F}(f)]$, where $g(\mathbf{k})$ is a

real-valued function associated with the two branches of the polariton kinetic energy $E_{L,U}(\mathbf{k})$ through [7,16]

$$g(\mathbf{k}) = \frac{\hbar^2 |\mathbf{k}|^2}{m(\mathbf{k})} = \frac{k^2}{2} \partial_k^2 E_{L,U}(\mathbf{k}) := g(k), \quad (2)$$

where $k = |\mathbf{k}|$ for $\mathbf{k} \in \mathbb{R}^d$ with $d = 2, 1$. Here $E_{L,U}(\mathbf{k}) = \hbar\omega_{L,U}(\mathbf{k})$ with $\omega_{L,U}(\mathbf{k})$ the two branches of the polariton dispersion [14], which vary significantly over $|\mathbf{k}|$ and the kinetic energy (2) depends on the $|\mathbf{k}|$ of the injected or spontaneously populated condensate polaritons generally in a nonparabolic way. In fact, one aim of the choice of (2) is so that the kinetic equation is no longer a monotonically increasing function with respect to $|\mathbf{k}|$, while $m(\mathbf{k}) = \frac{2\hbar^2}{\partial_k^2 E_{L,U}(\mathbf{k})} = \frac{2\hbar}{\partial_k^2 \omega_{L,U}(\mathbf{k})}$ can be interpreted as the effective velocity-dependent mass of the polariton, which can change sign with respect to $k = |\mathbf{k}|$. In fact, locally *fractional kinetic energies* can be implemented due to the *velocity-dependent mass* $m(\mathbf{k})$ that modifies the parabolic dispersion accordingly—e.g., a modification of the polariton condensate wave function due to effectively negative mass was recently shown experimentally [16].

In this paper, the whole spectrum of the lower polariton branch is considered while taking the dynamical behavior into account. We clarify the role of the generalized kinetic energy as it is particularly important for implementations above the inflection point and because several mathematically different forms of the kinetic energy have been used in similar scenarios, while neglecting the inherent mathematical inconsistencies of the corresponding predictions as secondary effects [17–19]. Current models catch aspects of the condensate wave function at localized \mathbf{k} in the regime when $|\mathbf{k}|$ is near zero, but the concept introduced here incorporates the mean-field treatment for more extended wave packets in \mathbf{k} space, while being the more accurate description even for localized wave packets. Concepts such as energy relaxation can be included in the partial differential equation (PDE) [11,19,20]. Numerically, we find that a time-splitting Fourier pseudospectral method [21,22] can be used to generate converging solutions, a method that will be presented in more detail in a later work.

*florian.pinsker@physics.ox.ac.uk

II. THEORETICAL BACKGROUND

84

85 Polaritons are quasiparticles consisting of excitons and cavity
86 photons within semiconductor microcavities which obey
87 Bose-Einstein statistics [14] and thus the potential to condense
88 into a single-particle mode [23]. Excitons are coupled pairs of
89 electrons and holes of oppositely charged spin-half particles in
90 a semiconductor held together by the Coulomb force between
91 them [15]. Excitons interact with light fields [24] and can form
92 integer spin-polariton quasiparticles in the strong-coupling
93 regime that are confined to the microcavity [25]. As polaritons
94 are 10^9 times lighter than rubidium atoms [23], condensation
95 is observed in CdTe/CdMgTe/GaAs microcavities [14,23,26]
96 and, recently, even at room temperature in flexible polymer-
97 based structures [27,28]. The basic Hamiltonian taking the
98 interaction between the cavity light modes and excitons into
99 account is stated in [14,15]. By diagonalizing this operator,
100 one gets the lower and upper polariton eigenvalues [15],

$$\omega_{L,U}(\mathbf{k}) = \frac{1}{2} \left\{ \omega_{\text{cav}}(\mathbf{k}) + \omega_{\text{exc}}(\mathbf{k}) \mp \sqrt{[\omega_{\text{cav}}(\mathbf{k}) - \omega_{\text{exc}}(\mathbf{k})]^2 + 4\Omega_R^2} \right\}. \quad (3)$$

101 The dispersion of the cavity photon is $\omega_{\text{cav}}(\mathbf{k}) = \frac{c}{n_0} \sqrt{q_z^2 + |\mathbf{k}|^2}$
102 with c the speed of light, $q_z = \frac{2\pi M}{l_z}$ the quantization in
103 the z direction, M the number of the quantized z mode
104 orthogonal to the \mathbf{k} plane, n_0 the refraction index between
105 the cavity mirrors, and l_z the cavity spacer length. The
106 dispersion of the exciton $\omega_{\text{exc}}(\mathbf{k}) \approx \omega_{\text{exc}}^0$, which can be
107 assumed as constant close to the center of the polariton
108 dispersion. $2\Omega_R$ is the minimum splitting of the two polariton
109 branches, which is obtained at $\omega_{\text{cav}}(\mathbf{k}) = \omega_{\text{exc}}(\mathbf{k})$. For
110 our investigation, we set $\hbar\omega_{\text{exc}}^0 = 1.557$ eV, the mass of
111 the cavity photon $m_{\text{cav}} \sim 10^{-4} - 10^{-5} m_e$, and the effective
112 exciton mass $m_{\text{exc}} \sim 0.1 - 1 m_e$, with m_e the electron mass
113 in accordance with recent results presented in [26]. When $|\mathbf{k}|$
114 is sufficiently small, $\omega_{\text{cav}}(\mathbf{k}) = \omega_{\text{cav}}^0 \sqrt{1 + \hbar|\mathbf{k}|^2 / (m_{\text{cav}} \omega_{\text{cav}}^0)} \sim$
115 $\omega_{\text{cav}}^0 [1 + \frac{\hbar|\mathbf{k}|^2}{2m_{\text{cav}} \omega_{\text{cav}}^0}] = \omega_{\text{cav}}^0 + \frac{\hbar|\mathbf{k}|^2}{2m_{\text{cav}}}$, with the notations $\omega_{\text{cav}}^0 =$
116 $\frac{c q_z}{n_0} = \frac{2\pi c M}{n_0 l_z}$ and the effective cavity photon mass $m_{\text{cav}} =$
117 $\frac{\hbar n_0 q_z}{c} = \frac{\hbar \omega_{\text{cav}}^0}{c^2 / n_0^2}$. Thus, when $|\mathbf{k}|$ is sufficiently small,
118 $\omega_{L,U}(\mathbf{k}) \sim \omega_{\pm}^0 \mp \sqrt{\Omega_R^2 + (\omega_{\pm}^0)^2} + \frac{\hbar|\mathbf{k}|^2}{4m_{\text{cav}}} [1 \mp \frac{\omega_{\pm}^0}{\sqrt{\Omega_R^2 + (\omega_{\pm}^0)^2}}] := \omega_{\text{lin}}(\mathbf{k})$ with
119 $\omega_{\pm}^0 = \frac{1}{2} [\omega_{\text{cav}}^0 \pm \omega_{\text{exc}}^0]$, which immediately implies that those
120 models based on the Gross-Pitaevskii equation (GPE) for
121 polariton condensates in the literature [14] are based on the
122 approximate dispersion relation $\omega_{\text{lin}}(\mathbf{k})$, i.e., *constant mass*.
123 On the other hand, when $|\mathbf{k}|$ is sufficiently large, $\omega_L(\mathbf{k}) \sim \omega_{\text{exc}}^0$
124 and $\omega_U(\mathbf{k}) \sim |\mathbf{k}| \sqrt{\hbar \omega_{\text{cav}}^0 / m_{\text{cav}}}$.

125 In Fig. 1(a), we show the kinetic energy of the lower and
126 upper branches of polariton $\hbar\omega_{L,U}(\mathbf{k})$, i.e., Eq. (3), the
127 exciton energy $\hbar\omega_{\text{exc}}(\mathbf{k}) \approx \hbar\omega_{\text{exc}}^0$, and the linear approximation
128 $\hbar\omega_{\text{lin}}(\mathbf{k})$, and in Fig. 1(b), we show the kinetic energy related
129 to Eq. (2). Figure 1(b) shows that locally fractional and
130 generalized quantum kinetic energies are present due to the
131 varying curvature of the effective mass—an example is given
132 for $s = 5/6$, which approximates the bottom of the polariton
133 dispersion at $k \sim 0$ to a higher accuracy than the parabolic
134 dispersion. The effective mass switches sign from positive
135 at $k < k_{\text{inf}}$ to negative at $k > k_{\text{inf}}$. In between, it becomes

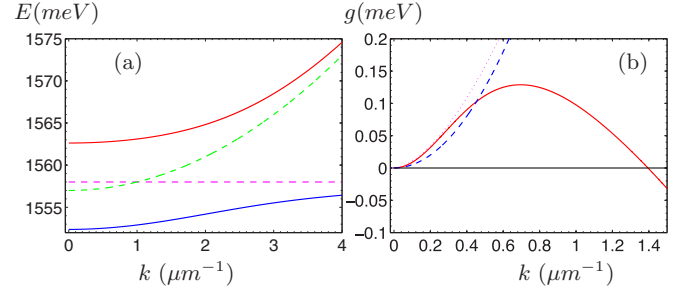


FIG. 1. (Color online) (a) Energy dispersions of the upper and lower polariton energy branch (solid lines), and the cavity (parabolic) and exciton (almost constant) dispersions (dashed lines). (b) Kinetic-energy prefactors $g(\mathbf{k})$ defined in Eq. (2), including velocity-dependent mass (solid line) compared with constant mass (dashed line) and fractional kinetic energy $|\mathbf{k}|^{5/3}$ (dotted line). The sign of the kinetic energy switches for velocity-dependent mass.

infinite on a circle centered around the origin at $k = 0$ in the two-dimensional (2D) \mathbf{k} plane—the inflection point $k = k_{\text{inf}} \sim 1.3952 \mu\text{m}^{-1}$. While models of coupled PDEs separating the photonic and the excitonic fraction have been discussed previously [29,30], here we present a unifying approach for the mean field of condensed polaritons resulting in a single nonlocal PDE as a realistic model of generalized fractional quantum mechanics in a highly controllable solid-state system.

III. GENERALIZED STATE EQUATION

Phenomenologically, the condensate wave function is governed by a generalized Gross-Pitaevskii equation with nonlocal kinetic interaction, damping, and pumping terms [11,13–15,17,18], which includes the effects of polariton self-interactions, polariton-reservoir interactions, and nonequilibrium properties such as gain and decay of condensate polaritons. An accurate quantum theory of polaritons is provided in [31]. While in the mean-field regime the spin of polaritons can become apparent through circular polarization of the driving light source or transverse-magnetic–transverse-electric (TM-TE) splitting, even spontaneously [26], we assume the spin coherent case for the introduction of the velocity-dependent mass of the lower branch (2) (see [7]) and include it mathematically, setting $q(\mathbf{r}) = \mathcal{F}^{-1}[g(\mathbf{k})]$. Thus the kinetic energy becomes $\mathcal{F}^{-1}[g(\mathbf{k}) \cdot \hat{f}] = \mathcal{F}^{-1}[\mathcal{F}(q) \cdot \mathcal{F}(f)] = q \star f$ up to a constant, with \star denoting a convolution. Consequently, the polariton state equation resembling a coherent driving scheme [14,32], by setting $\hbar = 1, m_e = 1$, reads as follows:

$$i\partial_t \psi(\mathbf{r}, t) = (1 - i\eta)q \star \psi(\mathbf{r}, t) + iP(\mathbf{r}, t) - i\gamma \psi(\mathbf{r}, t) + [\beta|\psi|^2 + V(\mathbf{r}, t) + \omega]\psi(\mathbf{r}, t), \quad (4)$$

where ω is a constant, β is the dimensionless self-interaction strength, $V(\mathbf{r}, t)$ is an external potential, $\gamma \geq 0$ is the loss rate of polaritons due to their decay, and $\eta \geq 0$ is the energy relaxation rate [33]. The coherent pumping field is [14,32]

$$P(\mathbf{r}, t) = P_0(\mathbf{r}) e^{i\mathbf{k}_i \cdot \mathbf{r}} e^{-i\omega_i t}, \quad (5)$$

with $P_0(\mathbf{r})$ denoting the pump profile amplitude, \mathbf{k}_i denoting the 2D pump wave vector, and $\omega_i = \omega_L(\mathbf{k}_i)$. Figure 1(a) shows

170 that locally close to the particular \mathbf{k}_i under consideration,
 171 fractional kinetic energies emerge and thus the presented
 172 model (4) includes, as a special case, a feasible implementation
 173 of (driven) fractional quantum mechanics. Via \mathbf{k}_i , we can
 174 choose experimentally at which particular \mathbf{k} the condensate
 175 wave function is formed on the dispersion in \mathbf{k} space.
 176 Alternatively, with incoherent driving schemes, one could
 177 control \mathbf{k} of the condensate by adjusting the spot size, which
 178 determines the final velocity of condensed polaritons [12].

179 IV. PLANE WAVES WITHOUT TRAPPING

180 Let us now present analytical plane-wave solutions with
 181 respect to the velocity-dependent mass of the polariton system
 182 with homogeneous pumping and no trapping. In Eqs. (4)
 183 and (5), we assume homogeneous pumping $P_0(\mathbf{r}) \equiv P_c$, with
 184 P_c a constant, and no external potential $V(\mathbf{r}, t) \equiv 0$. Then
 185 we can set an ansatz for the stationary solution $\psi(x, t) =$
 186 $\psi_c e^{i\mathbf{k}_i \cdot \mathbf{r}} e^{-i\omega_i t}$, with ψ_c being a constant. Substituting the ansatz
 187 into Eq. (4), we get

$$\begin{aligned} & [\omega_i - \omega - \beta|\psi_c|^2 + i\gamma - (1 - i\eta)(q \star e^{i\mathbf{k}_i \cdot \mathbf{r}})e^{-i\mathbf{k}_i \cdot \mathbf{r}}] \psi_c \\ & = iP_c. \end{aligned} \quad (6)$$

188 By using properties of the Fourier transform, we have

$$\begin{aligned} (q \star e^{i\mathbf{k}_i \cdot \mathbf{r}})e^{-i\mathbf{k}_i \cdot \mathbf{r}} &= \mathcal{F}^{-1}[\hat{q}(\mathbf{k})(2\pi)^d \delta(\mathbf{k} - \mathbf{k}_i)]e^{-i\mathbf{k}_i \cdot \mathbf{r}} \\ &= \hat{q}(\mathbf{k}_i) = g(\mathbf{k}_i). \end{aligned} \quad (7)$$

189 Hence,

$$[\omega_i - \omega - (1 - i\eta)g(\mathbf{k}_i) - \beta|\psi_c|^2 + i\gamma] \psi_c = iP_c. \quad (8)$$

190 This resembles an equation of the form

$$(\alpha_i + i\gamma_i - \beta|\psi_c|^2) \psi_c = iP_c \quad (9)$$

191 when introducing the abbreviations $\alpha_i = \omega_i - \omega - g(\mathbf{k}_i)$ and
 192 $\gamma_i = \gamma + \eta g(\mathbf{k}_i)$. When $\beta = 0$ and $P_c \neq 0$, Eq. (9) has a unique
 193 solution $\psi_c = \frac{iP_c}{\alpha_i + i\gamma_i}$ if either $\alpha_i \neq 0$ or $\gamma_i \neq 0$, and it has no
 194 solution if $\alpha_i = \gamma_i = 0$, e.g., no damping with $\gamma = \eta = 0$ and
 195 pumping with $\omega_i = g(\mathbf{k}_i)$ and $\omega = 0$. When $\beta \neq 0$, it has three
 196 solutions as

$$\psi_c^\pm = -\frac{(1 \pm i\sqrt{3})(\alpha_i + i\gamma_i)}{2\xi^{1/3}} - \frac{(1 \mp i\sqrt{3})\xi^{1/3}}{6\beta} \quad (10)$$

197 and

$$\psi_c^0 = \frac{\alpha_i + i\gamma_i}{\xi^{1/3}} + \frac{\xi^{1/3}}{3\beta}, \quad (11)$$

198 with $\xi = \frac{-27i\beta^2 P_c + \sqrt{-4(3\alpha_i\beta + 3i\gamma_i\beta)^3 - 729\beta^4 P_c^2}}{2}$.

199 The density $\rho_c^\pm = |\psi_c^\pm|^2$ tends to zero for $P_c \rightarrow 0$, which
 200 corresponds to no pumping of polaritons into the condensate,
 201 and it increases monotonically with P_c . The solutions are
 202 modified by the velocity-dependent mass (2) and the constant
 203 mass case is obtained by substituting $m(\mathbf{k}) \equiv m_c$, with m_c
 204 a constant. For the plane-wave scenario, respecting $m(\mathbf{k})$ implies
 205 including its value at \mathbf{k}_i of the dispersion [see Fig. 1(a)], which
 206 modifies the magnitude of the wave function (or the luminosity
 207 of the microcavity). Nonlocal effects can be expected in more
 208 general pumping schemes, as shown below.

V. LINEAR WAVES ANALYSIS

209 For the sake of simplicity, we shall restrict ourselves here
 210 to the illustrative case of a spatially homogeneous system, i.e.,
 211 $V(\mathbf{r}, t) \equiv 0$ in (4) under a coherent pump with $P_0(\mathbf{r}) \equiv P_c$, with
 212 P_c a constant and $\mathbf{k}_i = 0$ in (5). As shown in the previous sec-
 213 tion, Eq. (4) admits plane-wave solution $\psi_o(\mathbf{r}, t) = \psi_c e^{-i\omega_i^0 t}$
 214 and denotes $\rho_c = |\psi_c|^2$. To find the linearized elementary
 215 excitation equation around the plane wave $\psi_o(\mathbf{r}, t)$, taking
 216 an ansatz $\psi(\mathbf{r}, t) = [\psi_c + \delta\psi(\mathbf{r}, t) - \delta\psi^*(\mathbf{r}, t)]e^{-i\omega_i^0 t}$ with $\delta\psi$
 217 and $\delta\psi^*$ small perturbations and \bar{f} the complex conjugate
 218 of f , plugging it into (4), and keeping only up to linear
 219 terms in terms of $\delta\psi$ and $\delta\psi^*$ (by ignoring all high-order
 220 terms) [14,17], we obtain the Bogoliubov equation for the
 221 polariton field modulation $\delta\psi$ and $\delta\psi^*$ which reads
 222

$$\begin{aligned} i\partial_t \delta\psi &= (1 - i\eta)q \star \delta\psi + [\omega - \omega_i^0 + 2\beta\rho_c - i\gamma] \delta\psi \\ &+ \beta\bar{\psi}_c^2 \delta\psi^* + P_1, \end{aligned} \quad (12)$$

$$\begin{aligned} i\partial_t \delta\psi^* &= -(1 + i\eta)q \star \delta\psi^* - [\omega - \omega_i^0 + 2\beta\rho_c + i\gamma] \delta\psi^* \\ &- \beta\bar{\psi}_c^2 \delta\psi + \bar{P}_1, \end{aligned} \quad (13)$$

223 where $P_1 = iP_c + [\omega - \omega_i^0 + \beta\rho_c - i\gamma + (1 - i\eta)g(0)]\psi_c$.
 224 Assume ψ_c satisfies (8) with $\mathbf{k}_i = \mathbf{0}$, i.e., $\psi(\mathbf{r}, t)$ is a stationary
 225 state; then the inhomogeneous terms will disappear, i.e., $P_1 =$
 226 0 in (12) and (13). Choosing the Bogoliubov modes in a plane-
 227 wave form of wave vector \mathbf{k} as $\delta\psi(\mathbf{r}, t) = \delta\psi_{\mathbf{k}} e^{i\mathbf{k} \cdot \mathbf{r}} e^{-i\omega_{\text{Bog}}(\mathbf{k})t}$
 228 and $\delta\psi^*(\mathbf{r}, t) = \delta\psi_{\mathbf{k}}^* e^{i\mathbf{k} \cdot \mathbf{r}} e^{-i\omega_{\text{Bog}}(\mathbf{k})t}$, the above Bogoliubov
 229 equation reduces to an eigenvalue problem with its eigenvalue
 230 given by the so-called Bogoliubov dispersion of excitations,

$$\omega_{\text{Bog}}(\mathbf{k}) = -i\gamma_{\mathbf{k}} \pm \sqrt{\alpha_{\mathbf{k}}^2 - \beta^2 \rho_c^2}, \quad (14)$$

231 where $\gamma_{\mathbf{k}} = \gamma + \eta g(\mathbf{k})$ and $\alpha_{\mathbf{k}} = \omega - \omega_i^0 + g(\mathbf{k}) + 2\beta\rho_c$. The
 232 signs correspond to the positive and negative Bogoliubov
 233 branch and, as expected, the presence of the velocity-
 234 dependent mass adapts the excitation energy by a nonparabolic
 235 $|\mathbf{k}|$ dependence of the effective kinetic energy.

236 To consider the traveling-wave solution of the Bogoliubov
 237 equations (12) and (13), we set the ansatz $\delta\psi(\mathbf{r}, t) =$
 238 $\delta\phi(\mathbf{r} - \mathbf{v}t) := \delta\phi(\mathbf{r}')$ and $\delta\psi^*(\mathbf{r}, t) = \delta\phi^*(\mathbf{r} - \mathbf{v}t) := \delta\phi^*(\mathbf{r}')$,
 239 with $\mathbf{r}' = \mathbf{r} - \mathbf{v}t$ and $\mathbf{v} \in \mathbb{R}^2$ the traveling-wave velocity. By

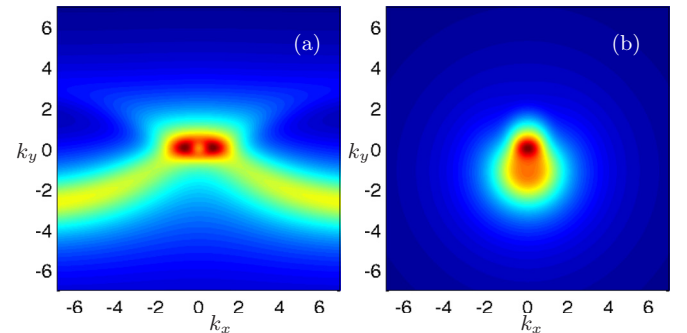


FIG. 2. (Color online) (a) $|\delta\psi_{\mathbf{k}}|$ including velocity dependence of the effective mass for parameters $v_x = 0$ and $v_y = 1$ in \mathbf{k} space. (b) $|\delta\psi_{\mathbf{k}}|$ for the same parameters but for constant mass. From zero magnitude (blue) to stronger magnitude (red, toward center of figure).

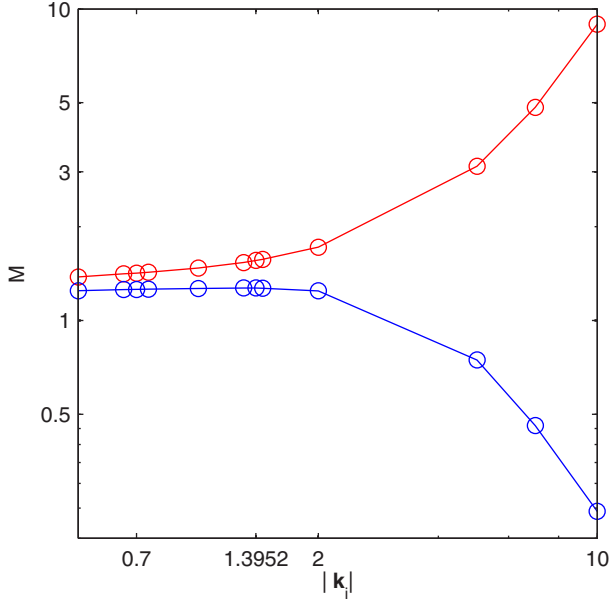


FIG. 3. (Color online) Converged mass M in both the velocity-dependent and constant mass model. The red line corresponds to the L^2 norm, including the velocity-dependent mass effect. The blue line corresponds to the constant mass model.

5 plugging the ansatz into the Bogoliubov equations (12) and (13), noticing $\partial_t \delta\psi(\mathbf{r}, t) = -(\mathbf{v} \cdot \nabla) \delta\phi(\mathbf{r}')$ and $\partial_t \delta\psi^*(\mathbf{r}, t) = -(\mathbf{v} \cdot \nabla) \delta\phi^*(\mathbf{r}')$, dropping the superscripts, and then taking the Fourier transform, we obtain, for $\delta\phi_{\mathbf{k}} = \mathcal{F}(\delta\phi)$ and $\delta\phi_{\mathbf{k}}^* = \mathcal{F}(\delta\phi^*)$ by taking $\psi_c = \sqrt{\rho_c}$, $\mu = \beta\rho_c$, $\mu_{\mathbf{k}} = \beta\rho_c + g(\mathbf{k})$, and $\omega = \omega_i^0 - \mu$,

$$(\mathbf{k} \cdot \mathbf{v}) \delta\phi_{\mathbf{k}} = (\mu_{\mathbf{k}} - i\gamma_{\mathbf{k}}) \delta\phi_{\mathbf{k}} + \mu \delta\phi_{\mathbf{k}}^* + \mathcal{F}(P_1)_{\mathbf{k}}, \quad (15)$$

$$(\mathbf{k} \cdot \mathbf{v}) \delta\phi_{\mathbf{k}}^* = -(\mu_{\mathbf{k}} + i\gamma_{\mathbf{k}}) \delta\phi_{\mathbf{k}}^* - \mu \delta\phi_{\mathbf{k}} - \mathcal{F}(\overline{P_1})_{\mathbf{k}}. \quad (16)$$

246 Solving the above system, we get

$$\delta\phi_{\mathbf{k}} = \frac{[(\mathbf{k} \cdot \mathbf{v}) + \mu_{\mathbf{k}} + i\gamma_{\mathbf{k}}] \mathcal{F}(P_1)_{\mathbf{k}} - \mu \mathcal{F}(\overline{P_1})_{\mathbf{k}}}{[(\mathbf{k} \cdot \mathbf{v}) + i\gamma_{\mathbf{k}}]^2 - \mu_{\mathbf{k}}^2 + \mu^2}. \quad (17)$$

247 This solution is a natural extension of the equilibrium atomic
248 BEC solutions presented in [34,35] and those for constant

mass discussed in [14]. In Fig. 2, we compare the solutions $\delta\phi_{\mathbf{k}}$ due to constant and velocity-dependent mass. For the sake of simplicity, we assume $\mathcal{F}(P_1)_{\mathbf{k}} \equiv 1$, $\gamma = 1$, $\mu = 1$, and $g(\mathbf{k})$ is given as described above. The results indicate a significant difference in the linear wave condensate dynamics, which, in particular, will be investigated numerically in more detail in the following section.

VI. NUMERICAL RESULTS IN 2D

Here we report numerical results for the model (4) with coherent pumping (5) in 2D under the *velocity-dependent mass* scenario with $E_L(\mathbf{k}) = \omega_L(\mathbf{k}) = \sqrt{1 + 2|\mathbf{k}|^2} - \sqrt{105.04 + 2|\mathbf{k}|^2}$ in (2), and, respectively, the *constant mass* scenario with $g(\mathbf{k}) = |\mathbf{k}|^2$ [in dimensionless form by setting $\hbar = 1$, $m_e = 1$, $\omega_{\text{cav}}^0 = 2$, and $m_{\text{cav}} = 1/4$ in Eq. (3)]. We take a Gaussian pump profile $P_0(\mathbf{r}) = A_0 \exp[-(|\mathbf{r} - \mathbf{d}|)^2/\sigma^2]$, where A_0 is the amplitude, \mathbf{d} denotes the position of the pump, and σ is its width. For coherent pumping, we always take $\omega_i = \omega_L(\mathbf{k}_i)$ in Eq. (5) and $\omega = 0$ in Eq. (4). The pumping vector is chosen as $\mathbf{k}_i = (a, a)/\sqrt{2}$ with $a \geq 0$ and the initial wave function is taken as $\psi_I(x, y) = \exp[-(x^2 + y^2)]$. The simulation results shown below are computed for $\eta = 0.05$, $\beta = 0.001$, $\gamma = 0.3$, $A_0 = 10$, $\sigma = 1$, and $\mathbf{d} = \mathbf{0}$ on a bounded computational domain $[-8, 8]^2$ with mesh size $h = 1/16$ in both the x and y direction and time step $\Delta t = 10^{-4}$ by an efficient and accurate numerical method [36]. The stationary state is obtained when $\|\rho^n - \rho^{n+1}\|_{\text{max}} \leq 10^{-8}$ is reached, where $\rho^n = |\psi^n|^2$ with ψ^n is the numerical solution at time $t = t_n = n\Delta t$. In order to quantify the dynamics of the solution, we define the mass at time t as $M(t) := \sqrt{\int_{\mathbb{R}^2} |\psi(\mathbf{r}, t)|^2 d\mathbf{r}}$. Over a long time, denoted by t_{∞} , both models converges to a stationary state of different L^2 norms $M(t_{\infty})$.

A. No external potential

Here we will present numerical results without external potential, i.e., $V(\mathbf{r}, t) \equiv 0$ in Eq. (4).

In Fig. 3, we show a comparison of the converged mass $M(t_{\infty})$ between the velocity-dependent and constant mass models. The mass of the condensate increases with $|\mathbf{k}_i|$ for the velocity-dependent mass model, while it decreases for the

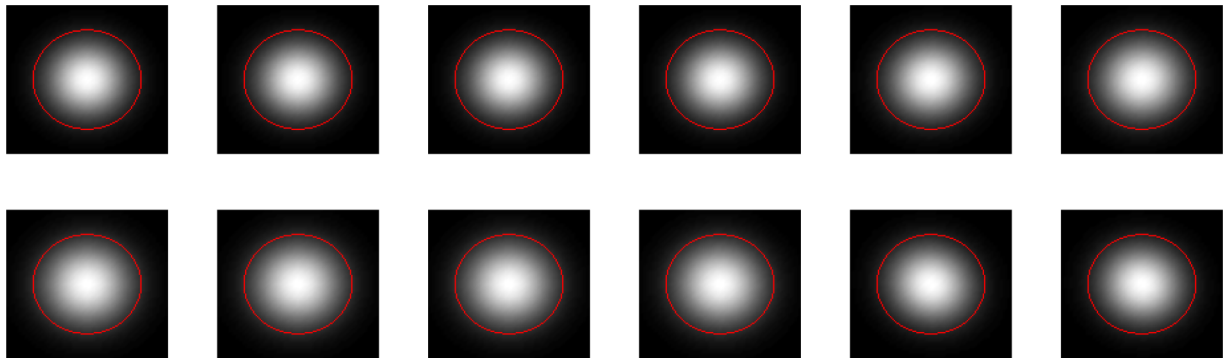


FIG. 4. (Color online) Comparison between the density profiles $\rho(\mathbf{r}, t_{\infty})$ generated by the velocity-dependent mass model: upper row $a = \{0, 0.7, 1.39, 2, 7, 10.38\}$ from the left to the right; and correspondingly in the lower row stemming from the constant mass model (brighter areas correspond to higher density).

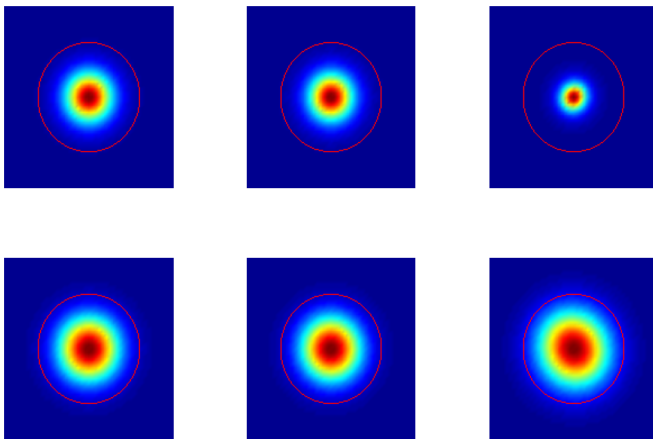


FIG. 5. (Color online) Comparison between the 2D density profiles due to a Gaussian pumping spot $\rho(\mathbf{r}, t_\infty) = |\psi|^2$ simulated by the $m(\mathbf{k})$ model: upper line $a = \{0, 1.39, 10.38\}$ from the left to the right; and correspondingly in the lower line ρ stemming from the constant mass model. Blue corresponds to lower densities and red is associated with higher densities. The red line is a guide for the eye.

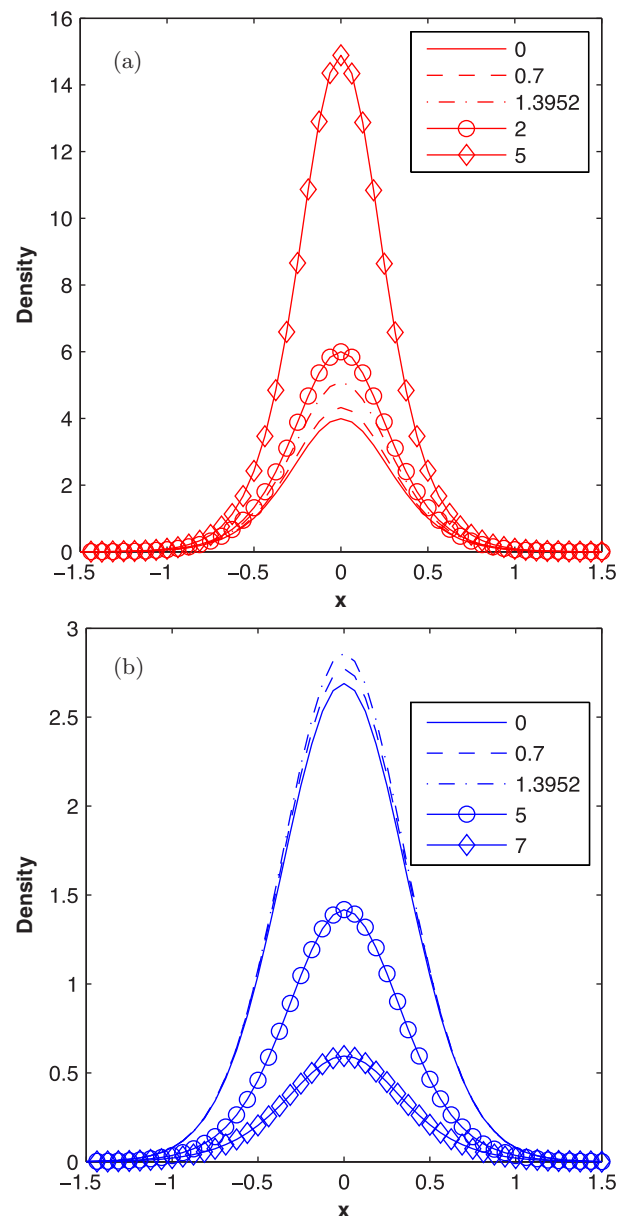


FIG. 7. (Color online) The red line in (a) corresponds to the x -axis slice plot of the density profile for the velocity-dependent mass model. The blue line in (b) corresponds to the constant mass model.

constant mass case. A qualitative comparison of the density profiles is presented in Fig. 4. The impact of effective attraction between polaritons is less visible than shown in Fig. 5 where an external trap has been applied.

B. Harmonic potential

Here we will present numerical results with a harmonic potential, i.e., $V(\mathbf{r}, t) = 20|\mathbf{r}|^2$ in Eq. (4).

In Fig. 6(a), we show a comparison of the total mass of a perturbed condensate wave function as it varies in time for a fixed \mathbf{k}_i , i.e., $a = 1.3952$. The constant mass implies oscillations of the L^2 norm/total density over time, while the velocity-dependent mass acts as a damping term, as shown in Fig. 6(a). To elucidate the differences in the total mass of the condensate, we show in Fig. 6(b) a comparison for different $\mathbf{k}_i (\mu\text{m}^{-1})$. Similarly, as $|\mathbf{k}_i|$ increases, $M(t_\infty)$ monotonically increases for the $m(\mathbf{k})$ model while it decreases for the classic model, hence offering an experimentally feasible test of the theory (4). In addition, we present the qualitative results of the converged density along the x axis in Fig. 7.

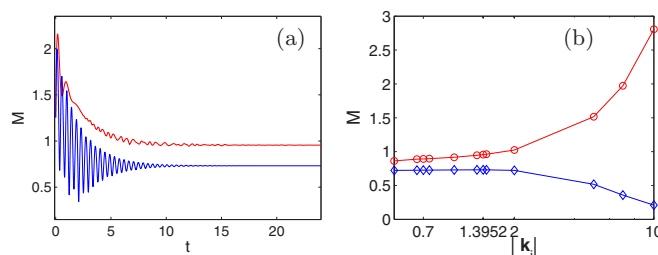


FIG. 6. (Color online) Polaritons in a harmonic potential trap. (a) Red line corresponds to the $M(t)$, including the $m(\mathbf{k})$ effect over time t with $[t] = ps$. The blue line corresponds to the constant mass model. (b) The red line corresponds to $M(t_\infty)$, including the $m(\mathbf{k})$ effect. The blue line corresponds to the constant mass model. Units are $[\mathbf{k}_i] = \mu\text{m}^{-1}$.

C. Mexican hat potential

Here we will present numerical results with a Mexican hat potential, i.e., $V(\mathbf{r}, t) = |\mathbf{r}|^2 + 50 \exp(-|\mathbf{r}|^2/0.2)$ in Eq. (4).

In Fig. 8, we show a comparison of the density distributions of stationary states for different \mathbf{k}_i with $a \in \{0, 10, 38\}$. We observe that the density cloud/luminosity for velocity-dependent mass contracts as $|\mathbf{k}_i|$ increases—a behavior analogous to attractive atomic BEC in traps [37–40]. Instead of negative/repulsive self-interactions, the negative mass induces a relative sign between the kinetic energy and the still repulsive self-interactions (4), leading to the observed contraction consistent with the experimental results in [16]. The diameter of the ring-shaped condensate increases with $|\mathbf{k}_i|$ for the $m(\mathbf{k})$

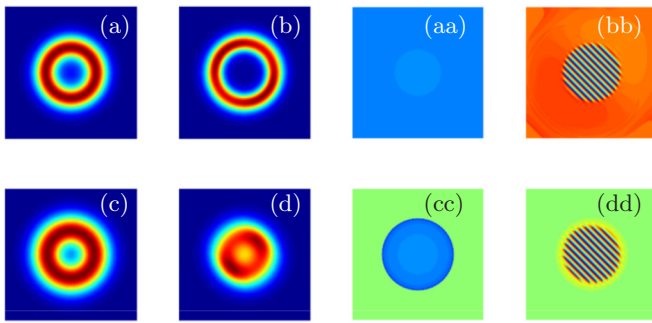


FIG. 8. (Color online) Comparison between the converged densities governed by the $m(\mathbf{k})$ model in the upper row: (a) density and (aa) phase for $a = 0$ and (b) density and (bb) phase for $a = 10.38$. Correspondingly, in the lower row, (c),(d) density and (cc),(dd) phase stemming from the classic model. Blue corresponds to lower densities and red is associated with higher densities.

parabolic nonlinear SE-type models previously used. Via a feasible coherent pumping scheme—driving the polariton to condense at a chosen single point of its dispersion—one can effectively switch between different points of the energy dispersion, enabling tests of the effects of velocity-dependent mass. The importance of the in-plane momentum for the emerging polariton condensate shown in explicit analytical expressions and linear waves analysis suggests significant different dynamical behavior. Numerical simulations in 2D scenarios, for which a time-splitting Fourier pseudospectral method has been developed, reveal evident differences in the predictions for the polariton condensate to classic results. The dynamics shows a suppression of total density oscillations due to the velocity-dependent mass, with total mass increasing for larger k , while classic mean-field models predict a reduction in mass. The latter phenomenon is a feasible test of the theory presented here. In addition, condensates forming above the inflection point show attractive-type density profiles, in accordance with the observations in [16]. While the coherent driving scheme utilized in this paper defines the phase and suppresses the spontaneous emergence of excitations such as vortices or dark and bright solitons, incoherent driving schemes may reveal interesting pattern formation in the future.

ACKNOWLEDGMENTS

F.P. acknowledges financial support from a Schrödinger Fellowship at the University of Oxford and the NQIT Project No. EP/M013243/1. W.B. acknowledges support by the Ministry of Education of Singapore Grant No. R-146-000-196-112. Y.Z. acknowledges support by the ANR-FWF Project Lodiquas No. ANR-11-IS01-0003, the ANR Project Moonrise No. ANR-14-CE23-0007-01, and the Natural Science Foundation of China Grants No. 91430103 and No. 11471050. We are very grateful to Peter Cristofolini, Jesus Sierra, and Peter Markowich for stimulating discussions and a keen interest in this topic.

VII. CONCLUSIONS

We have identified the polariton condensate wave functions with those of fractional quantum mechanics by considering the velocity-dependent mass of polaritons in the governing PDE. More generally, because the \mathbf{k} -dependent kinetic energy of the polariton condensate deviates significantly from the parabolic form, different phenomena could be observed. Remarkably, for $k \sim 0$, a fractional nonlinear Schrödinger-type equation is the more accurate model compared to the classic

- [1] N. Laskin, *Phys. Lett. A* **268**, 298 (2000).
- [2] N. Laskin, *Phys. Rev. E* **62**, 3135 (2000).
- [3] M. Jeng, S.-L.-Y. Xu, E. Hawkins, and J. M. Schwarz, *J. Math. Phys.* **51**, 062102 (2010).
- [4] C. Klein, C. Sparber, and P. A. Markowich, *Proc. R. Soc. A* **470**, 20140364 (2014).
- [5] X. Guo and M. Xu, *J. Math. Phys.* **47**, 082104 (2006).
- [6] J. Dong and M. Xu, *J. Math. Phys.* **48**, 072105 (2007).
- [7] M. S. Dresselhaus (unpublished).
- [8] G. Tosi *et al.*, *Nat. Phys.* **8**, 190 (2012).
- [9] F. Pinsker and T. Alexander, *Proc. Roy. Soc. A* **471**, 20150210 (2015).
- [10] C. Leyder, T. C. H. Liew, A. V. Kavokin, I. A. Shelykh, M. Romanelli, J. Ph. Karr, E. Giacobino, and A. Bramati, *Phys. Rev. Lett.* **99**, 196402 (2007).
- [11] A. Dreismann *et al.*, *Nat. Phys.* **11**, 8770 (2014).
- [12] E. Wertz *et al.*, *Nat. Phys.* **6**, 860 (2010).
- [13] F. Pinsker and H. Flayac, *Phys. Rev. Lett.* **112**, 140405 (2014).
- [14] I. Carusotto and C. Ciuti, *Rev. Mod. Phys.* **85**, 299 (2013).
- [15] H. Deng, H. Haug, and Y. Yamamoto, *Rev. Mod. Phys.* **82**, 1489 (2010).
- [16] M. Sich *et al.*, *Nat. Photon.* **6**, 50 (2012).
- [17] M. Wouters and I. Carusotto, *Phys. Rev. Lett.* **99**, 140402 (2007).
- [18] J. Keeling and N. G. Berloff, *Phys. Rev. Lett.* **100**, 250401 (2008).
- [19] M. Wouters, T. C. H. Liew, and V. Savona, *Phys. Rev. B* **82**, 245315 (2010).
- [20] S. Choi, S. A. Morgan, and K. Burnett, *Phys. Rev. A* **57**, 4057 (1998).
- [21] W. Bao, D. Jaksch, and P. A. Markowich, *J. Comput. Phys.* **187**, 318 (2003).
- [22] W. Bao and Y. Cai, *Kinet. Relat. Mod.* **6**, 1 (2013).
- [23] J. Kasprzak *et al.*, *Nature (London)* **443**, 409 (2006).
- [24] J. J. Hopfield, *Phys. Rev.* **112**, 1555 (1958).
- [25] C. Weisbuch *et al.*, *Phys. Rev. Lett.* **69**, 3314 (1992).

- [26] H. Ohadi, A. Dreismann, Y. G. Rubo, F. Pinsker, Y. delValle-InclanRedondo, S. I. Tsintzos, Z. Hatzopoulos, P. G. Savvidis, and J. J. Baumberg, *Phys. Rev. X* **5**, 031002 (2015).
- [27] J. D. Plumhof, *et al.*, *Nat. Mater.* **13**, 247 (2013).
- [28] S. Christopoulos, G. Baldassarri Höger von Högersthal, A. J. D. Grundy, P. G. Lagoudakis, A. V. Kavokin, J. J. Baumberg, G. Christmann, R. Butté, E. Feltin, J.-F. Carlin, and N. Grandjean, *Phys. Rev. Lett.* **98**, 126405 (2007).
- [29] T. C. H. Liew, A. V. Kavokin, and I. A. Shelykh, *Phys. Rev. B* **75**, 241301 (2007).
- [30] H. Flayac, D. D. Solnyshkov, and G. Malpuech, *Phys. Rev. B* **83**, 045412 (2011).
- [31] D. Racine and P. R. Eastham, *Phys. Rev. B* **90**, 085308 (2014).
- [32] M. Wouters and I. Carusotto, *Phys. Rev. B* **75**, 075332 (2007).
- [33] S. Choi, S. A. Morgan, and K. Burnett, *Phys. Rev. A* **57**, 4057 (1998).
- [34] G. E. Astrakharchik and L. P. Pitaevskii, *Phys. Rev. A* **70**, 013608 (2004).
- [35] Y. G. Gladush, L. A. Smirnov, and A. M. Kamchatnov, *J. Phys. B* **41**, 165301 (2008).
- [36] W. Bao, Q. Tang, and Y. Zhang (unpublished).
- [37] F. Dalfovo, S. Giorgini, L. P. Pitaevskii, and S. Stringari, *Rev. Mod. Phys.* **71**, 463 (1999).
- [38] F. Pinsker, *Ann. Phys.* **362**, 726 (2015).
- [39] I. Carusotto and C. Ciuti, *Phys. Rev. Lett.* **93**, 166401 (2004).
- [40] C. Ciuti and I. Carusotto, *Phys. Status Solidi B* **242**, 2224 (2005).